Journal of Non-Crystalline Solids 596 (2022) 121878

Contents lists available at ScienceDirect

Journal of Non-Crystalline Solids

journal homepage: www.elsevier.com/locate/jnoncrysol

The effect of impurities in zirconium on the formation and mechanical properties of $Zr_{55}Cu_{30}Al_{10}Ni_5$ metallic glass

Ye Liu [a], Ziliang Yin [a], Hongbo Lou [a,*], Tao Liang [a,b], Hongliang Dong [a], Dazhe Xu [a], Chao Song [a], Qifan Wang [a,b], Songyi Chen [a], Xin Zhang [a], Xiehang Chen [a], Zhidan Zeng [a], Qiaoshi Zeng [a,*]

[a] Center for High Pressure Science and Technology Advanced Research (HPSTAR), Pudong, Shanghai, 201203, People's Republic of China
[b] Jiangsu Key Laboratory of Advanced Metallic Materials, School of Materials Science and Engineering, Southeast University, Nanjing, 211189, People's Republic of China

ARTICLE INFO

Keywords:
Bulk metallic glass
Impurities
Glass-forming ability
Plasticity

ABSTRACT

Minor alloying has been developed as an effective method to modify and optimize various properties of bulk metallic glasses (BMG). In this work, as inevitable minor alloying elements, two major impurities, hafnium (Hf) and oxygen (O) were quantitatively confirmed to co-exist in two zirconium (Zr) raw materials with different grades of impurities. The effects of these two impurities on the thermal properties, crystallization behavior, glass-forming ability (GFA), and mechanical properties of the nominal $Zr_{55}Cu_{30}Al_{10}Ni_5$ BMG were systematically studied. The O impurity was found to promote the formation of the $Al_5Ni_3Zr_2$ intermetallic compound phase, which could account for the poor GFA, thermal stability, and plasticity associated with BMGs with higher O content in the Zr raw material. In contrast, although the impurity of Hf has a much higher content than O, a negligible effect of Hf on the $Zr_{55}Cu_{30}Al_{10}Ni_5$ BMG was revealed. These findings were further confirmed by deliberately adding extra O and Hf with designed contents into the $Zr_{55}Cu_{30}Al_{10}Ni_5$ BMG. Our results clarify the effects of different impurities in Zr raw materials on the Zr-based BMG and will help guide industrial production and applications of Zr-based BMGs.

1. Introduction

Bulk metallic glasses (BMGs) with the capabilities of combining superior properties of both conventional glasses and metallic alloys are promising to have widespread applications [1, 2]. Various studies have shown that the properties of BMGs are sensitive to minor alloying elements [3–10]. Other than intended additions of minor alloying elements, it has been found that common impurities in metallic raw materials such as oxygen (O) can significantly affect the glass forming ability (GFA), plasticity, relaxation, and thermal stability of BMGs [11–16], which might hold the key to address the diversity in GFA and plasticity for BMGs with the same nominal compositions reported by different research groups [17–20].

In industrial production, the purity of raw materials is critical, which significantly affects the final contents of impurities in designed alloys and the costs of products [12, 14]. Thus, it is essential to clarify the relationship between the properties of produced BMGs and the various common impurities in their raw materials. Zr-based BMG is one of the most widely studied BMG systems with good GFA and is also promising for various industrial applications [21], although the major element zirconium (Zr) is challenging to be purified. It had been believed that a large amount of oxygen (more than 1000 ppm) was poison for GFA and the plasticity of BMGs [4]. However, Wang *et al.* [7] and Wu *et al.* [8] recently found that a considerable amount of oxygen could still elevate the plasticity of BMGs. In addition, Qiao *et al.* found that substituting Zr with Hf can substantially increase the GFA in a Zr-based BMG [5]. These results inspire us to re-think the problems regarding impurities in Zr-based BMGs. Hf (naturally an intergrowth element with Zr) and O (strong affinity for Zr atoms [13]) are inevitable to co-exist as main impurity elements in Zr raw materials. It calls for a systematic study on the comprehensive effects of Hf and O impurities in Zr-based BMGs rather than separate studies on individual impurity as previously reported. The questions such as which impurity plays a dominant role, how to choose the appropriate impurity grade of raw materials for a specific application of Zr-based BMGs, etc., also remain unclear.

In this work, two Zr raw materials with different grades of impurities

* Corresponding authors.
E-mail addresses: hongbo.lou@hpstar.ac.cn (H. Lou), zengqs@hpstar.ac.cn (Q. Zeng).

https://doi.org/10.1016/j.jnoncrysol.2022.121878
Received 22 June 2022; Received in revised form 9 August 2022; Accepted 19 August 2022
Available online 23 August 2022

were used to synthesize the $Zr_{55}Cu_{30}Al_{10}Ni_5$ BMG. Detailed compositional characterization with ultrahigh accuracy was carried out to measure the contents of all common impurities in the synthesized BMGs. Hf and O were found to be two major impurities in two raw materials, respectively. Further, we systematically investigated the effects of Hf and O impurities on various properties of the two BMGs. We confirmed that the O impurity at the hundreds of ppm level plays a dominant role and degrades almost all properties of the $Zr_{55}Cu_{30}Al_{10}Ni_5$ BMG, while Hf impurity has no dramatic effect.

2. Materials and methods

2.1. Sample preparation

The master ingots of the $Zr_{55}Cu_{30}Al_{10}Ni_5$ (nominal composition in atomic ratio) alloy were prepared by arc-melting a mixture of Zr, Cu (99.999%), Al (99.999%), and Ni (99.995%) metals under a Ti-gettered argon atmosphere. Extra samples with intended doping of O or Hf for comparison were synthesized by adding CuO powder (99.995%) or Hf metal (99.99%), respectively. Two raw Zr materials with different purity levels were purchased from ZhongNuo Advanced Material (Beijing) Technology Co., Ltd. (China) as starting materials. Specifically, the price of the high-purity grade Zr (99.89%, low Hf content) is ~500 USD per kilogram, and the other low-purity grade Zr (98.17%, high Hf content) is only ~75 USD per kilogram, which are named as HP-Zr and LP-Zr hereafter for convenience. Chemical uniformity was ensured by flipping and multiple re-melting (at least four times) of all the master ingots. The cylindric samples with a diameter of ~2 mm, plate-shaped samples with a sectional dimension of $\sim 1 \times 10$ mm^2 and triangular plate samples were all prepared using the copper-mold suction casting technique in an arc-melting system.

2.2. Materials characterization

The typical impurity species and contents in Zr raw materials and the $Zr_{55}Cu_{30}Al_{10}Ni_5$ BMGs were measured by the inductively coupled plasma optical emission spectroscopy (ICP-OES) using ICAP 6300 spectrometer (Thermo Fisher Scientific, USA). The contents of light elements, including oxygen, carbon, and sulfur, were measured using the inert gas fusion method (ONH836, LECO) and the high-frequency infrared CS instrument (CS844, LECO). The amorphous nature was analyzed by x-ray diffraction (XRD, Malvern Panalytical Empyrean) with the Cu-K_α radiation and a beam size of 1×10 mm^2. All the BMG sample surfaces were carefully polished before XRD measurements to avoid artifacts in the thin surface layer due to chemical contamination or heterogeneous nucleation. Synchrotron XRD experiments were performed at the beamline 13W1 at the Shanghai Synchrotron Radiation Facility (SSRF), China. The synchrotron x-ray wavelength was 0.3066 Å, and the beam size was $\sim 45 \times 5$ μm^2. The software Dioptas [22] was used to integrate the two-dimensional diffraction images into one-dimensional XRD patterns. Thermal properties were examined using differential scanning calorimetry (DSC, PerkinElmer DSC 8500) at constant heating rates ranging from 0.083 to 1.67 K s^{-1} after instrumental correction. The second heating curve of crystallized sample served as the baseline. The melting behavior of all the samples was measured using another high-temperature DSC (Netzsch DSC 404F) with a constant heating rate of 0.33 K s^{-1}. Sample densities were measured by Archimedes method using an analytical balance with a density kit (Mettler Toledo XSE105DU, resolution of 0.01 mg). Each sample was measured at least ten times for good statistics. Standard deviation was used as the experimental error when calculating the mean density value from multiple measurements.

2.3. Mechanical testing

Uniaxial compression tests were carried out on an Instron 5966 machine at room temperature under a constant displacement rate of 1×10^{-4} s^{-1}. Testing samples had a diameter of ~2 mm and an initial aspect ratio (height:diameter) of ~2:1. Before testing, both ends of samples were ground by a custom device designed to make sure they were parallel and perpendicular to the loading axis. The fracture surfaces and the lateral surfaces of samples after testing were examined by scanning electron microscope (SEM, FEI Versa 3D).

Nanoindentation tests were performed using an instrumented nano Indenter (G200, Keysight, USA) equipped with a standard Berkovich diamond indenter at room temperature. Sample surfaces were carefully ground and polished to a mirror finish before tests. The nanoindentation measurements were carried out under a displacement-control mode with a maximum load of 20 mN at a strain rate of 0.05 s^{-1}. The elastic modulus and nano-hardness were calculated by fitting the load-displacement (p-h) curve using the Oliver-Pharr method [23].

Table 1
Contents of impurities in two zirconium raw materials measured by ICP-OES. The error is less than 1 ppm. The value less than 0.2 or 0.5 means that the content of these elements in materials are below the detection limit.

Name	Zr purity (wt.%)	Impurity elements' content (ppm in mass ratio)					
		Hf	Fe	Cr	Mn	Mo	Ti
LP-Zr	98.17	18,000	0.21	<0.2	<0.2	<0.5	1.5
HP-Zr	99.89	2.6	3.9	0.29	<0.2	<0.5	3.4

3. Results and discussion

3.1. Characterization of impurities and their effect on the thermal process

The ICP is a powerful tool for trace element analysis and is widely used because of its low detection limits (part per billion, ppb) [24]. Except for some light elements (e.g., hydrogen), almost all common elements can be detected. Firstly, the two raw materials of Zr named as HP-Zr and LP-Zr were dissolved, then the contents of their impurity elements, including Hf, Fe, Cr, Mn, Mo, Si, and Ti, were measured by the ICP method (results were summarized in Table 1). Secondly, the contents of similar impurity elements were measured using ICP method in the $Zr_{55}Cu_{30}Al_{10}Ni_5$ BMGs rods (2 mm in diameter) prepared using the two different Zr raw materials under the same experimental conditions (results summarized in Table 2). In addition, the contents of light elements, including O, C, and S, in the two BMGs were also measured. The main impurities in the two BMGs prepared with LP-Zr and HP-Zr are Hf and O, respectively, while the other impurities are minor and negligible. Specifically, the Hf impurity in the BMG with LP-Zr accounts for 1.237 wt.% (mass ratio) and is three orders of magnitude higher than the Hf content in the BMG with HP-Zr. The content of the Hf impurity in BMGs shows good inheritance from the Zr raw materials, in which the content of the Hf impurity in LP-Zr raw materials is 1.800 wt.%. The content of O in the BMG with HP-Zr is 695 ppm (part per million in mass ratio) and is nearly three times of that in the BMG with LP-Zr. By calculating, surprisingly, we can find the contents of O impurity in the HP-Zr raw material is nearly 700 ppm higher than the LP-Zr. The actual purity of the LP-Zr and HP-Zr raw materials are experimentally determined to be 98.17 wt.% and 99.89 wt.%, respectively. According to the compositional analysis above, the actual compositions of the two BMGs synthesized with LP-Zr and HP-Zr are $Zr_{54.39}Cu_{30}Al_{10}Ni_5O_{0.11}Hf_{0.50}$ and $Zr_{54.67}Cu_{30}Al_{10}Ni_5O_{0.33}$ (atomic ratio), respectively, which will be named as Zr(Hf) and Zr(O) BMGs, respectively, hereafter for convenience.

The amorphous nature of the Zr(Hf) and Zr(O) BMGs was confirmed by synchrotron XRD, shown in Fig. 1(a). The position of the first diffraction peak (q_1) of the Zr(Hf) BMG is 2.632 $Å^{-1}$ by fitting the peak using a Gauss function and is slightly larger (by 0.15%) than that of the Zr(O) BMG, which is 2.628 $Å^{-1}$. According to the power law between density and the q_1 [25, 26], the density of the Zr(Hf) BMG would be

Table 2
Contents of impurities in the Zr(Hf) and Zr(O) BMGs. The unit is ppm in mass ratio. The errors of the contents of O, C, and S elements are less than 1%. Other elements were measured by ICP-OES and the errors are less than 1 ppm.

Name	O	C	S	Hf	Fe	Cr	Mn	Mo	Ti	Si	True composition (at.%)
Zr(Hf)	232	40	70	12,370	57	439	11	5	74	43	$Zr_{54.39}Cu_{30}Al_{10}Ni_5O_{0.11}Hf_{0.50}$
Zr(O)	695	33	80	12	172	442	11	13	119	98	$Zr_{54.67}Cu_{30}Al_{10}Ni_5O_{0.33}$

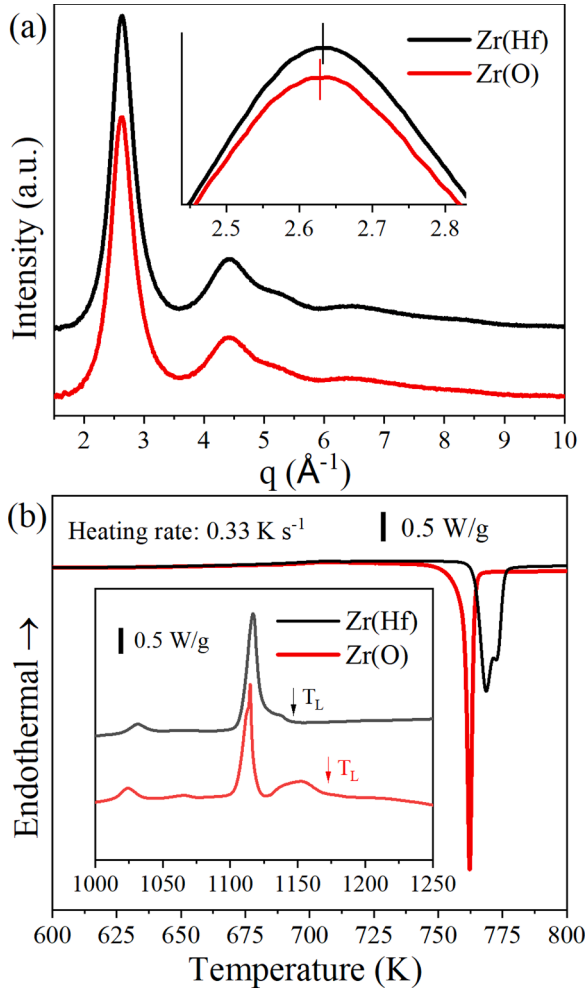

Fig. 1. Characterization of the glass nature of the Zr(Hf) and Zr(O) BMGs. (a) Synchrotron XRD patterns showing typical amorphous features of the as-cast Zr(Hf) and Zr(O) BMGs with a diameter of 2 mm. (b) the DSC traces of the Zr (Hf) and Zr(O) BMGs heated to 800 K and 1250 K (the inset) at a heating rate of 0.33 K s^{-1}.

higher than the Zr(O) BMG. The measured density of the Zr(Hf) and Zr (O) BMGs (ρ_a) is 6.824 g cm^{-3} and 6.766 g cm^{-3}, respectively, consistent with the estimation of a slightly higher density of Zr(Hf) than Zr(O) based on their XRD peak positions. DSC measurements of both BMG were conducted to investigate the effect of the Hf and O impurities on their thermal properties. Fig. 1(b) and the inset show the DSC traces of Zr(Hf) and Zr(O) BMGs obtained from as-cast samples with a heating rate of 0.33 K s^{-1}. Different crystallization behavior is observed in DSC traces, i.e., the Zr(Hf) BMG shows multiple crystallization peaks while the Zr(O) BMG only has a single crystallization peak. During melting, one more peak appears around 1150 K for the Zr(O) BMG (see the inset). The characteristic temperatures, including glass transition temperature (T_g), crystallization onset temperature (T_x), and liquidus temperature (T_l), determined by the crossing point temperature of the extrapolated line [27], are listed in Table 4. Both T_g and T_x of the Zr(Hf) BMG are

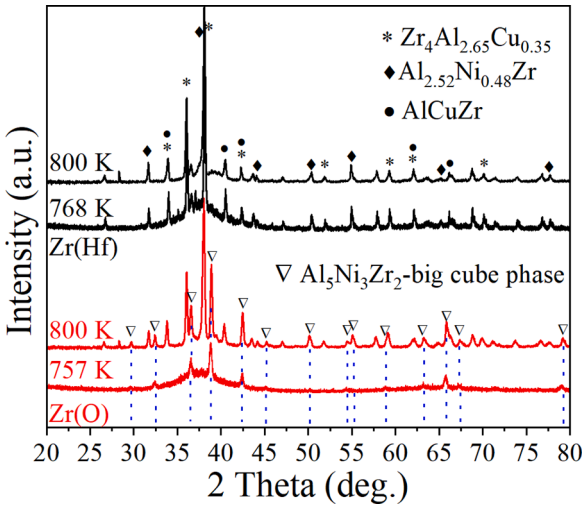

Fig. 2. Ex-situ study of crystallization products of the Zr(Hf) and Zr(O) BMGs. The XRD patterns of the Zr(Hf) BMG quenched from 768 K and 800 K and the Zr(O) BMG quenched from 757 K and 800 K. The heating rate and cooling rate are 0.33 K s^{-1} and 0.83 K s^{-1}, respectively.

higher than those of the Zr(O) BMG, suggesting higher thermal stability of the Zr(Hf) BMG than the Zr(O) one. The characteristic temperatures T_g and T_x are all close to the values previously reported in the literature [28]. The T_l of the Zr(O) BMG is 1173 K and higher than that (1147 K) of the Zr(Hf) BMG.

To further explore their difference in crystallization behavior, both BMGs were heated to the temperatures around and above (800 K) their T_x and then cooled down to the room temperature immediately to get the initial and complete crystallization products. The temperature when the crystallization fraction reached 15% (calculated by enthalpy change during crystallization) was used as the reference annealing temperature for producing the initial crystallization products. The XRD patterns in Fig. 2 reveal the different crystallized products of the Zr(Hf) and Zr(O) BMGs with two different degrees of crystallinity. For the Zr(Hf) BMG, the products of partially crystallized sample quenched from 768 K are the same as the fully crystallized sample quenched from 800 K. Most of the Bragg XRD peaks in these two samples of Zr (Hf) can be identified as $Zr_4Al_{2.65}Cu_{0.35}$ (Pearson's crystal number #1,005,084), $Al_{2.52}Ni_{0.48}Zr$ (PDF#01–5951), and AlCuZr (PDF#18–3885) phases, which is not consistent with the crystal phases reported previously in some literature [29–32]. This discrepancy may be associated with their different levels of various impurities and or different crystallinity. More interestingly, the partially crystallized product of the Zr(O) BMG quenched from 757 K can be identified as the $Al_5Ni_3Zr_2$ intermetallic compound phase (PDF#54–0437), which is a cube phase with the space group of *Fm3m* and a large unit cell (lattice constant $a = 1.204$ nm and a low density of 5.63 g cm^{-3}). With temperature increases, the $Al_5Ni_3Zr_2$ phase persists even when the Zr(O) BMG is fully crystallized at 800 K. Other phases of the Zr(O) sample quenched from 800 K are exactly the same as the three crystallization phases of the Zr(Hf) BMG. The $Al_5Ni_3Zr_2$ phase is likely the origin of the extra melting peak in the Zr(O) BMG in Fig. 1(b). These results indicate that the $Zr_{55}Cu_{30}Al_{10}Ni_5$ BMGs with different impurities show different crystallization behavior and products. Notably, the enhanced O impurity promotes the formation of the $Al_5Ni_3Zr_2$ phase in

Table 3
Density measurement of the alloys. The ρ_a and ρ_c are the average density of amorphous and crystallized alloys, respectively, measured by the Archimedes method. The error is less than 0.1%.

Name	ρ_a (g cm^{-3})	ρ_c (g cm^{-3})	$(\rho_c-\rho_a)/\rho_a$
Zr(Hf)	6.824 ± 0.001	6.846 ± 0.009	0.32%
Zr(O)	6.766 ± 0.002	6.796 ± 0.007	0.44%

the Zr(O) BMG, which could also explain the observation of the $Al_5Ni_3Zr_2$ phase in some previous studies on the crystallization of Zr-based BMGs [31, 32]. Dramatic effects of O doping on the crystallization products were also reported before, however, the specific crystal phase and its crystallinity may vary due to the different O contents and synthesis and or post-fabrication treatment conditions [33–35].

Microstructure dictates the properties of materials, and BMGs are no exception to this relationship. Based on computer simulations, many parameters were proposed to bridge the gap between the local microstructure and physical properties in BMGs, such as soft spots, local fivefold symmetry, local yield stress, and local atomic configuration [36–39]. Some of those local structural features have been observed by advanced experimental technologies [40–43] and correlated with properties such as thermal ultra-stability and local hardness fluctuation [44, 45]. Therefore, it is reasonable to speculate that the effect of minor impurities on the BMGs could also be attributed to their difference in local structures. For the Zr(O) BMG, the unexpected crystallization product ($Al_5Ni_3Zr_2$ phase) suggests its distinct local structure from that of Zr(Hf) BMG. Considering the low density of the $Al_5Ni_3Zr_2$ phase and cluster hypothesis [46], it is speculated that the O atoms promote the formation of local low-density zones with clusters close to the nuclei of the $Al_5Ni_3Zr_2$ phase, therefore, resulting in the precipitation of $Al_5Ni_3Zr_2$ phase in crystallization. This speculation is also consistent with the observation that Zr(O) BMG shows a reduction of 0.85% in the overall density compared with the Zr(Hf) BMG (Table 3). Previous studies also found "big cube phases" induced by minor O addition in Zr-based BMGs [47, 48]; thus, the feature that big cube phases lower thermal stability could be general in Zr-based BMGs. For the Zr(Hf) BMG, on the other hand, the Hf impurity has a marginal effect on the local structure because the Hf atoms usually play a similar role as the Zr atoms in BMGs [20].

3.2. Effect of impurities on the GFA

After several decades of studies, many parameters were proposed to be related to the GFA, such as the interval supercooled liquid region ($\Delta T_x = T_x$-T_g), the reduced glass transition temperature ($T_{rg} = T_g/T_L$), and the γ parameter ($\gamma = T_x/(T_g+T_L)$) [49–51]. The ΔT_x, T_{rg}, and γ parameters of the two BMGs were all calculated and summarized in Table 4.

There is a negligible difference in ΔT_x between the Zr(Hf) and Zr(O) BMGs, however, both T_{rg} and γ of the Zr(Hf) BMG are higher than the Zr (O) BMG, which indicates the higher GFA of the Zr(Hf) than the Zr(O) BMG. Furthermore, DSC traces with different heating rates ranging from 0.083 to 1.67 K s^{-1} were measured on both samples. The apparent activation energies of T_g, T_x, and T_p (the temperature of crystallization peak) were determined from the linear slope of the Kissinger plot [52]. The fitting values are listed in Table 4. The Zr(Hf) BMG has a close value of E_g with the Zr(O) BMG. In contrast, the E_x and E_p of Zr(Hf) BMG are 291.33 and 265.66 kJ mol^{-1}, respectively, which are higher than those of the Zr(O) BMG (272.95 and 256.43 kJ mol^{-1}, respectively). The activation energies of T_x and T_p are usually associated with the crystal-nucleation and crystal-growth processes, respectively [53, 54]. The smaller values of the E_x and E_p mean a lower ability to resist crystal nucleation and growth, which are in line with the worse GFA of the Zr (O) BMG [55].

Developing centimeter-sized BMG is important for further industrial application [21]. It has been reported the $Zr_{55}Cu_{30}Al_{10}Ni_5$ BMG has a critical size of 20 mm in diameter using a conventional casting technique [56]. Fig. 3(a) shows the XRD patterns of the Zr(Hf) and Zr(O) BMG plate samples with a cross-section of 1 × 10 mm^2 (see in the inset). The Zr(Hf) BMG is fully amorphous, while the Zr(O) BMG contains crystal phases as indicated by the emerging Bragg peaks, which can be indexed as the $Al_5Ni_3Zr_2$ phase and ZrO phase. Usually, the critical size of BMG is defined as the maximum diameter of fully amorphous BMG rods. Zhang et al. developped a wedge-shaped mold method to evaluate GFA, and

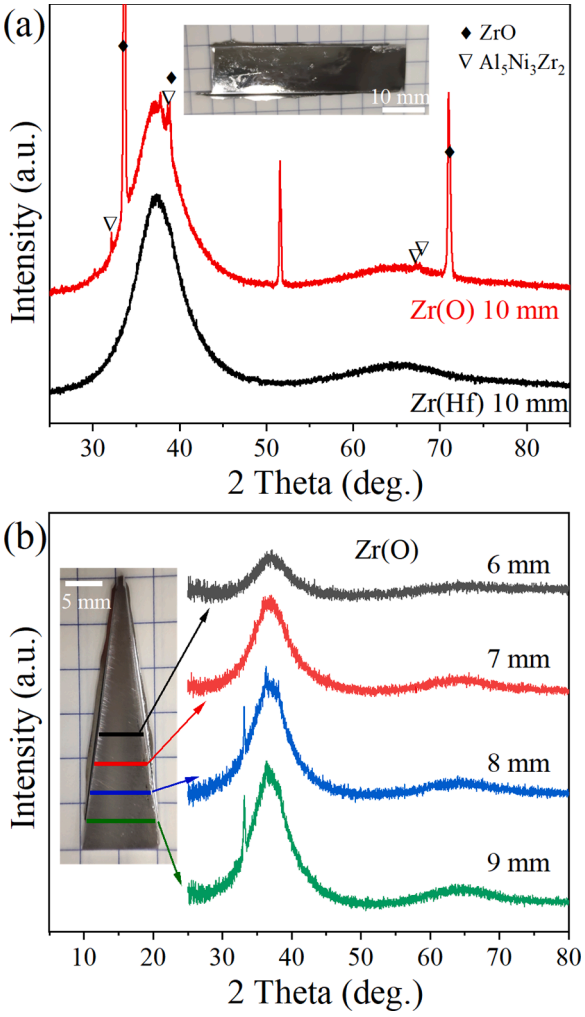

Fig. 3. Glass forming ability of the $Zr_{55}Cu_{30}Al_{10}Ni_5$ BMG prepared with two different purity grades of Zr raw materials. (a) XRD patterns of the Zr (Hf) and Zr(O) plate samples with a sectional dimension of 1 × 10 mm^2. (b) XRD mapping of the Zr(O) BMG with triangular shape.

Table 4
Thermal properties of the Zr(Hf) and Zr(O) BMGs.

Name	T_g (K)	T_x (K)	ΔT (K)	T_l (K)	T_{rg}	γ	E_g (kJ mol^{-1})	E_x (kJ mol^{-1})	E_p (kJ mol^{-1})
Zr(Hf)	665	764	99	1147	0.580	0.422	171 ± 9	291 ± 8	266 ± 11
Zr(O)	659	759	100	1173	0.563	0.414	171± 19	272 ± 5	256 ± 6

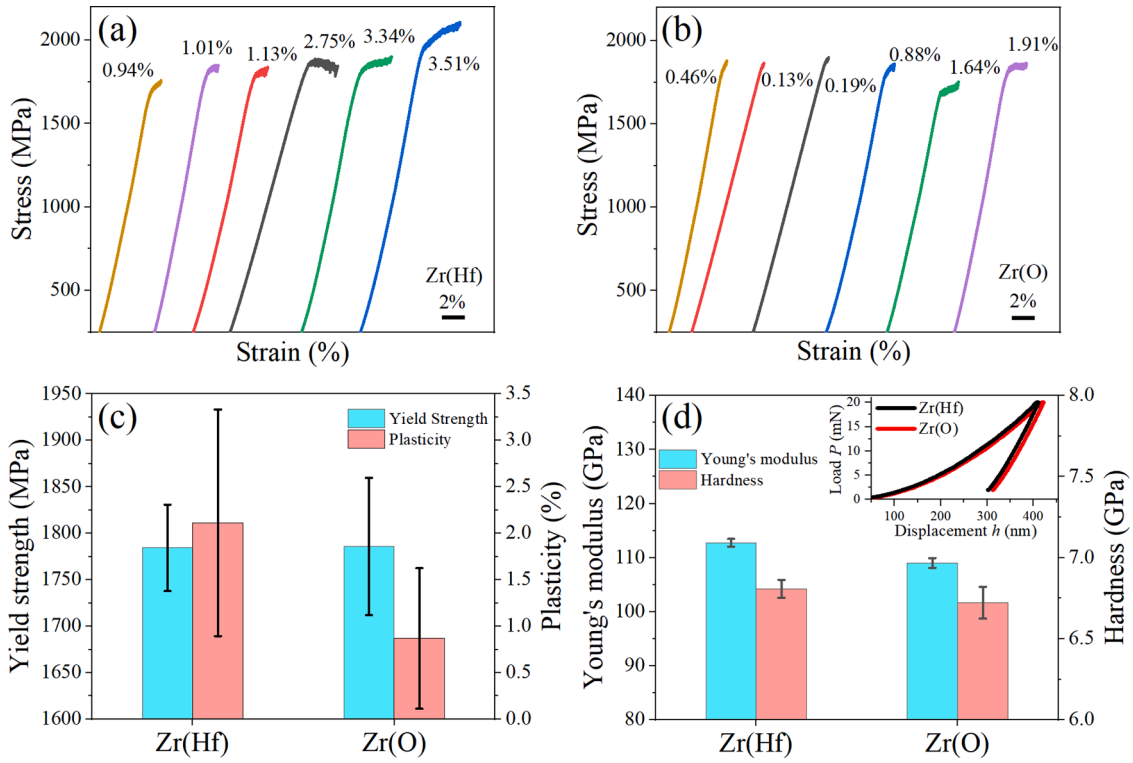

Fig. 4. Mechanical properties of the Zr(Hf) and Zr(O) BMGs. Engineering stress-strain curves of the as-cast Zr(Hf) (a) and Zr(O) (b) BMGs under uniaxial compression. (c) The average value of yield strength and plasticity of the two BMGs; (d) The average value of Young's modulus and hardness of the Zr(Hf) and Zr(O) BMGs. The inset show typical load-displacement curves of the two samples.

found that the maximum size of fully amorphous regions in wedge-shaped samples can be a good estimation of their critical sizes [57]. Based on this, we further simplify the mold to a triangular plate with a thickness of ~1 mm. Fig. 3(b) shows the XRD patterns at different positions of the triangular sample of the Zr(O) BMG. The maximum size of the fully amorphous region in the Zr(O) BMG is ~7 mm and smaller than the Zr(Hf) BMG, which has a maximum size of more than 10 mm. Apparently, O impurities degrade the GFA more severely than Hf impurity, although O impurity has one order less content than Hf impurity in the Zr-BMGs.

Atomic packing efficiency has been proved to be an effective indicator for the GFA of BMGs in both simulations and experiments [58–60]. Li et al. described that a small density change upon crystallization could be used to determine the ease of glass formation [59]. The density of fully crystallized samples (ρ_c) of the Zr(Hf) and Zr(O) BMGs were measured and summarized in Table 3. It is found that the density change upon crystallization, $(\rho_c\text{-}\rho_a)/\rho_a$, of the Zr(Hf) BMG is 0.32%, which is smaller than that (0.44%) of the Zr(O) BMG. Therefore, this result suggests higher atomic packing efficiency in the Zr(Hf) BMG. Previous research also pointed out that the big cube phase formed in Zr-based BMGs always causes worse GFA even with a low content of oxygen such as 900 ppm [47, 48], supporting our scenario of the $Al_5Ni_3Zr_2$ big cube phase in the Zr(O) BMG.

3.3. Effect of impurities on the mechanical properties

Fig. 4(a) and Fig. 4(b) show the engineering stress-strain curves of the Zr(Hf) and Zr(O) BMGs. To have better statistics, each composition was tested under uniaxial compression six times. According to the stress-strain curves, the Zr(Hf) BMG has better plasticity and the highest strain reaches 3.51%. The average yield strength and plasticity of the Zr(Hf) and Zr(O) BMGs are compared in Fig. 4(c). The average yield strength of the Zr(Hf) and the Zr(O) BMGs are 1784 MPa and 1785 MPa, respectively, which are almost identical. However, the average plasticity of the

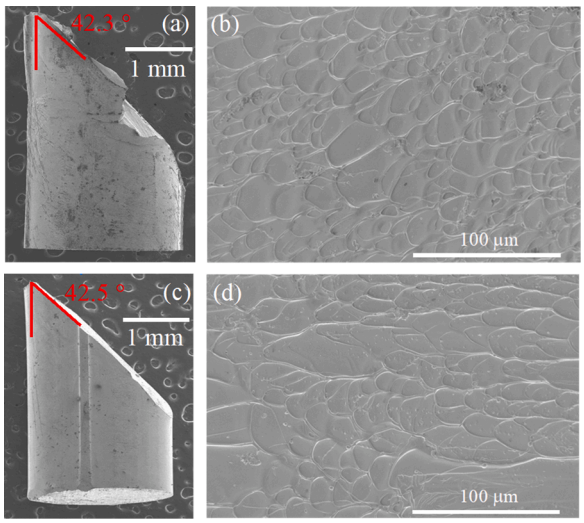

Fig. 5. Morphology analysis after uniaxial compression tests. The lateral surface micrographs of the Zr(Hf) (a) and Zr(O) (c) BMGs and the fracture surface morphologies for the Zr(Hf) (b) and Zr(O) (d) BMGs. The fracture angle in (a) and (c) are 42.3° and 42.5°, respectively.

Zr(Hf) BMG is 2.11%, which is much higher than the value (0.86%) of the Zr(O) BMG. Furthermore, to measure the Young's modulus and hardness, the nanoindentation tests were performed on both BMGs. The representative load-displacement (p-h) curves are shown in the inset of Fig. 4(d). Ten indents were tested on each sample, and the average value of Young's modulus and hardness were summarized in Fig. 4(d). The Zr (Hf) BMG has higher Young's modulus (112.7 GPa) and hardness (6.81 GPa) than those (109.0 GPa and 6.72 GPa, respectively) of the Zr(O) BMG. Roughly, these values of both samples are still close to the

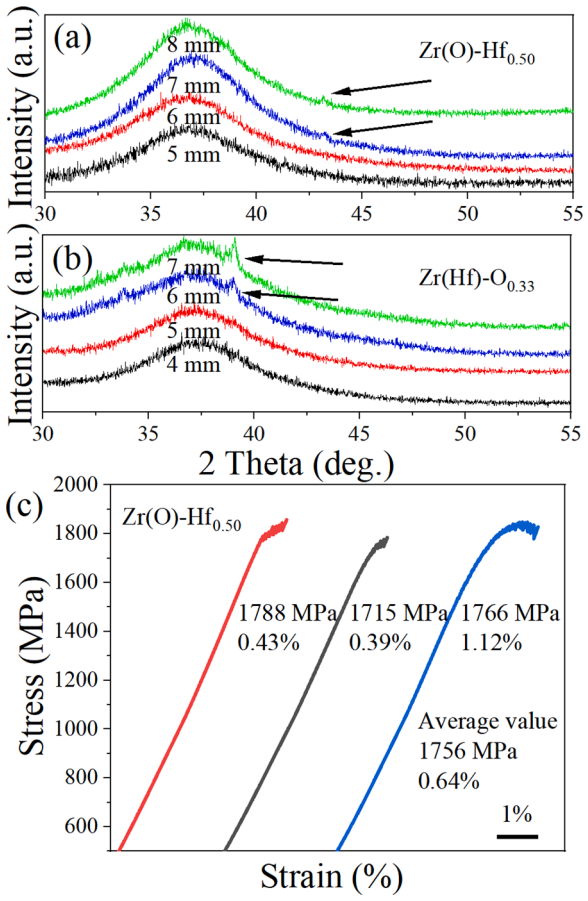

Fig. 6. Comparison of the effects of Hf and O impurity on the GFA and plasticity in the $Zr_{55}Cu_{30}Al_{10}Ni_5$ BMGs. XRD mapping of Zr(O)-$Hf_{0.50}$ (a) and Zr(Hf)-$O_{0.33}$ (b) BMGs with triangular shapes. (c) Engineering stress-strain curves of the Zr(O)-$Hf_{0.50}$ BMG.

previous reports by Aji et al. [61]. The local low-density zone related to the precursor clusters of $Al_5Ni_3Zr_2$ phase may account for the lower modulus and hardness in the Zr(O) BMG.

The plastic deformation of BMGs is mainly carried by narrow shear bands, whose proliferation and propagation dictate plasticity of BMGs. The fracture morphology of the Zr(Hf) and Zr(O) BMGs were observed by SEM, shown in Fig. 5. It can be seen from Fig. 5(a) and 5(c) that the Zr(Hf) BMG shows numerous and denser shear bands on the lateral surface compared with the Zr(O) BMG, indicating a more ductile feature in the Zr(Hf) BMG. The macroscopic views of the Zr(Hf) and Zr(O) BMGs show that shear failure has occurred at an angle of 42.3° and 42.5° with the compressive loading axis. In Fig. 5(b) and 5(d), the sheared fracture surface of the Zr(Hf) BMG also presents a denser dimple-like structure than the Zr(O) BMG. It is believed that dimple-like patterns result from the local softening of melting within the shear bands induced by the release of high stored energy during the instantaneous fracture [62]. Larger plasticity indicates more energy was released during the fracture process, causing denser patterns. The width of each dimple were counted and the calculated average width of dimples in the Zr(Hf) (Fig. 5(b)) and Zr(O) (Fig. 5(d)) BMGs are 11.8 ± 4.4 μm and 17.2 ± 5.6 μm, respectively. Such sizes are consistent with typical Zr-based BMGs [63]. Previous work reported that the yield strength increases when the size of the dimple in fracture surface increases in BMGs [63, 64], and our results also show a slight increase of yield strength in Zr(O) BMG.

The shear transformation zone (STZ) model proposed by Argon has been widely used to analyze the plasticity in metallic glasses [65]. The shear band grows in STZ and can interact with each other to stop breaking in metallic glasses [66]. Zhou et al. found that the STZ volume decreases with oxygen addition up to 3500 ppm, which depresses the growth of shear bands in Zr-based BMGs [9]. In our work, the oxygen content in the Zr(O) BMG is ~700 ppm. Thus, the lower plasticity caused by O impurity is also expected in the Zr(O) BMG according to the STZ perspective. Samavatian et al. [67] reported the plasticity of the as cast $Zr_{55}Cu_{30}Al_{10}Ni_5$ BMG is 1.9%, which is quite close to the plasticity (2.11%) observed in our Zr(Hf) BMG. The results indicate that the Hf impurity in Zr doesn't affect the plasticity of the $Zr_{55}Cu_{30}Al_{10}Ni_5$ BMG, while the O impurity could significantly decrease the plasticity.

3.4. Which impurity plays a dominant role?

The above results suggest that the O impurity in Zr has more evident effect than the Hf impurity on the $Zr_{55}Cu_{30}Al_{10}Ni_5$ BMG, but other possible factors could not be excluded. The intended minor addition of O and Hf impurities into the two Zr-based BMGs (making their composition identical) could be a straightforward way to verify our conclusions on the distinct effects of O and Hf impurities [4]. According to the actual compositions of the two Zr-based BMGs determined in this work (Table 2), extra Hf impurity (0.50 at.%) was added to the Zr(O) BMG to prepare the sample with a composition of $Zr_{54.17}Cu_{30}Al_{10}Ni_5O_{0.33}$-$Hf_{0.50}$ and the new sample was named Zr(O)-$Hf_{0.50}$. Similarly, extra O impurity (0.22 at.%) was added to the Zr(Hf) BMG to prepare the sample with a composition of $Zr_{54.17}Cu_{30}Al_{10}Ni_5O_{0.11}Hf_{0.50}$-$O_{0.22}$ and the new sample was named Zr(Hf)-$O_{0.33}$. The triangular samples of the Zr(O)-$Hf_{0.50}$ and Zr(Hf)-$O_{0.33}$ BMGs were prepared. Fig. 6(a) and 6(b) show the XRD mapping of the two triangular samples, and the arrows inside point to the crystalline Bragg peaks, from which we can find the maximum size of the Zr(O)-$Hf_{0.50}$ BMG is 6 mm, and the Zr(Hf)-$O_{0.33}$ BMG is 5 mm. Their maximum sizes are smaller than the Zr(Hf) BMG but close to the Zr(O) BMG in Fig. 3. The maximum size decreases slightly from 7 mm in Zr(O) BMG to 6 mm in Zr(O)-$Hf_{0.50}$ BMG, which evidence the marginal effect of Hf addition. In contrast, a significant role of O impurity was revealed as the maximum size decreases from more than 10 mm in the Zr(Hf) BMG down to 5 mm in the Zr(Hf)-$O_{0.33}$ BMG upon addition of 0.22 at.% of O impurity. It is worth noting that the crystallization products of the Zr(O)-$Hf_{0.5}$ and Zr(Hf)-$O_{0.33}$ BMGs are the same as the Zr(O) BMG, which means that the $Al_5Ni_3Zr_2$ phase always forms when the content of O impurity is up to 0.33 at.%. These results demonstrate that 0.50 at.% of Hf addition has a minimal effect on the GFA of the Zr-based BMG while 0.33 at.% of O addition can significantly degrade the GFA.

Fig. 6(c) shows the stress-strain curves of the Zr(O)-$Hf_{0.50}$ BMG during uniaxial compression. The average yield strength and plasticity of the Zr(O)-$Hf_{0.50}$ BMG are 1756 MPa and 0.64%, respectively, and both are lower than the values of the Zr(Hf) BMG in Fig. 4(a). This result suggests that once a small amount of O (0.33 at.%) impurity exists in the system, the plasticity will show a huge reduction in the $Zr_{55}Cu_{30}Al_{10}Ni_5$ BMG, while the 0.5 at% of Hf impurity shows very little influence in plasticity. Apparently, O impurity in Zr raw materials plays a more dominant role than Hf impurity in two of the most important properties, i.e., the GFA and plasticity, in the $Zr_{55}Cu_{30}Al_{10}Ni_5$ BMG.

4. Conclusion

The following conclusions have been inferred from the above investigation:

(1) By accurate compositional characterization, Hf and O were found to be the major impurities in two Zr raw materials with different grades of purity, which are the dominant contribution to the contents of impurities in final Zr-based BMGs.
(2) The O impurity was found to promote the formation of the $Al_5Ni_3Zr_2$ intermetallic compound phase, which suppresses the thermal stability, GFA, plasticity, Young's modulus, and hardness of the $Zr_{55}Cu_{30}Al_{10}Ni_5$ BMG. In contrast, although the impurity of

Hf has a much higher content than O, a negligible effect of Hf on the $Zr_{55}Cu_{30}Al_{10}Ni_5$ BMG properties was revealed.

(3) By deliberately adding O and Hf with designed contents into the two $Zr_{55}Cu_{30}Al_{10}Ni_5$ BMGs (synthesized with two different Zr raw materials) to make their real compositions identical, the dominant role O plays was verified, which suggests the O impurity in Zr raw materials need to be carefully estimated while high purity Zr raw materials with less Hf is unnecessary by considering its high cost and high content of O impurity.

Our results clarify the effects of Hf and O impurities in Zr raw materials on the Zr-based BMG and will help guide industrial production and applications of Zr-based BMGs with optimized properties but less cost.

CRediT authorship contribution statement

Ye Liu: Conceptualization, Methodology, Investigation, Formal analysis, Writing – review & editing. **Ziliang Yin:** Investigation, Formal analysis. **Hongbo Lou:** Writing – review & editing, Supervision. **Tao Liang:** Investigation, Formal analysis. **Hongliang Dong:** Investigation. **Dazhe Xu:** Investigation, Formal analysis. **Chao Song:** Investigation. **Qifan Wang:** Investigation. **Songyi Chen:** Investigation. **Xin Zhang:** Formal analysis. **Xiehang Chen:** Formal analysis. **Zhidan Zeng:** Resources, Supervision. **Qiaoshi Zeng:** Conceptualization, Resources, Writing – review & editing, Supervision, Funding acquisition.

Declaration of competing interest

The authors declare that they have no known competing financial interests or personal relationships that could have appeared to influence the work reported in this paper.

Data Availability

Data will be made available on request.

Acknowledgement

The authors acknowledge financial support from the National Natural Science Foundation of China (Grants No. 51871054 and No. U1930401). XRD experiments were performed at beamlines 13W1 and 15U1 of Shanghai Synchrotron Radiation Facility (SSRF), China.

References

[1] M. Ashby, A. Greer, Metallic glasses as structural materials, Scr. Mater 54 (2006) 321–326.
[2] W.H. Wang, C. Dong, C.H. Shek, Bulk metallic glasses, Mater. Sci. Eng. R Rep. 44 (2004) 45–89.
[3] Z.P. Lu, C.T. Liu, Role of minor alloying additions in formation of bulk metallic glasses: a Review, J. Mater. Sci. 39 (2004) 3965–3974.
[4] W. Wang, Roles of minor additions in formation and properties of bulk metallic glasses, Prog. Mater. Sci. 52 (2007) 540–596.
[5] D. Qiao, A. Peker, Enhanced glass forming ability in Zr-based bulk metallic glasses with Hf Addition, Intermetallics 24 (2012) 115–119.
[6] D.W. Ding, J. Tan, A.H. Cai, Y. Liu, H. Wu, Q. An, P.W. Li, Y. Zhang, Q. Yang, Effect of Ti addition on properties of Zr54Al10.2Ni9.4Cu26.4 glass forming alloy, J. Alloys Compd. 864 (2021).
[7] T. Wang, Q. Hou, L. Zhang, Enhanced heterogeneity and plasticity in a Zr - Cu – Al bulk metallic glass with micro-addition of oxygen, Mater. Sci. Eng. A 831 (2022).
[8] Y. Wu, D. Cao, Y. Yao, G. Zhang, J. Wang, L. Liu, F. Li, H. Fan, X. Liu, H. Wang, X. Wang, H. Zhu, S. Jiang, P. Kontis, D. Raabe, B. Gault, Z. Lu, Substantially enhanced plasticity of bulk metallic glasses by densifying local atomic packing, Nat. Commun. 12 (2021) 6582.
[9] W.H. Zhou, F.H. Duan, Y.H. Meng, C.C. Zheng, H.M. Chen, A.G. Huang, Y.X. Wang, Y. Li, Effect of alloying oxygen on the microstructure and mechanical properties of Zr-based bulk metallic glass, Acta Mater 220 (2021).
[10] L. Yu, J. Tang, H. Wang, Y. Wang, J. Qiao, M. Apreutesei, B. Normand, Corrosion behavior of bulk (Zr58Nb3Cu16Ni13Al10)100-xYx (x = 0, 0.5, 2.5 at.%) metallic glasses in sulfuric acid, Corros. Sci. 150 (2019) 42–53.
[11] D.Q.Z.B. Zhang, M.X. Pan, R.J. Wang, W.H. Wang, Metallic plastics based on misch metals, J. Non·Cryst. Solids 352 (2006) 5687–5690.
[12] J.L. Cheng, G. Chen, C.T. Liu, Y. Li, Innovative approach to the design of low-cost Zr-based BMG composites with good glass formation, Sci. Rep. 3 (2013) 2097.
[13] Y.X. Wang, H. Yang, G. Lim, Y. Li, Glass formation enhanced by oxygen in binary Zr–Cu system, Scr. Mater. 62 (2010) 682–685.
[14] P. Błyskun, P. Maj, T. Kozieł, K. Pajor, T. Kulik, Zirconium purity influence on the critical diameter and thermal indicators of the Zr48Cu36Al9Ag7 alloy, J. Non·Cryst. Solids 509 (2019) 80–87.
[15] S. Sohrabi, M.C. Ri, H.Y. Jiang, L. Gu, P. Wen, Y.H. Sun, W.H. Wang, Prominent role of chemical heterogeneity on cryogenic rejuvenation and thermomechanical properties of La–Al–Ni metallic glass, Intermetallics 111 (2019).
[16] K. Pajor, T. Kozieł, G. Cios, P. Błyskun, P. Bała, A. Zielińska-Lipiec, Glass forming ability of the Zr 50 Cu 40 Al 10 alloy with two oxygen levels, J. Non·Cryst. Solids 496 (2018) 42–47.
[17] D. Xu, B. Lohwongwatana, G. Duan, W.L. Johnson, C. Garland, Bulk metallic glass formation in binary Cu-rich alloy series Cu100-xZrx (x=34, 36, 38.2, 40 at.%) and mechanical properties of bulk Cu64Zr36 glass, Acta Mater 52 (2004) 2621–2624.
[18] T. Mei-Bo, Z. De-Qian, P. Ming-Xiang, W. Wei-Hua, Binary Cu–Zr Bulk Metallic Glasses, Chin. Phys. Lett., 21 (2004) 901–903.
[19] D. Wang, Y. Li, B.B. Sun, M.L. Sui, K. Lu, E. Ma, Bulk metallic glass formation in the binary Cu–Zr system, Appl. Phys. Lett. 84 (2004) 4029–4031.
[20] A. Inoue, W. Zhang, Formation, thermal stability and mechanical properties of Cu-Zr and Cu-Hf binary glassy alloy rods, Mater. Trans. JIM 45 (2004) 584–587.
[21] J.Y. Zhang, Z.Q. Zhou, Z.B. Zhang, M.H. Park, Q. Yu, Z. Li, J. Ma, A.D. Wang, H. G. Huang, M. Song, B.S. Guo, Q. Wang, Y. Yang, Recent development of chemically complex metallic glasses: from accelerated compositional design, additive manufacturing to novel applications, Materi. Futures 1 (2022), 012001.
[22] C. Prescher, V.B. Prakapenka, DIOPTAS: a program for reduction of two-dimensional X-ray diffraction data and data exploration, High Press. Res 35 (2015) 223–230.
[23] W.C. Oliver, G.M. Pharr, An improved technique for determining hardness and elastic modulus using load and displacement sensing indentation experiments, J. Mater. Res. 7 (1992) 1564–1583.
[24] J.W. Olesik, Elemental analysis using ICP-OES and ICP/MS, Anal. Chem. 63 (1991) 12A–21A.
[25] Q. Zeng, Y. Kono, Y. Lin, Z. Zeng, J. Wang, S.V. Sinogeikin, C. Park, Y. Meng, W. Yang, H.K. Mao, W.L. Mao, Universal fractional noncubic power law for density of metallic glasses, Phys. Rev. Lett. 112 (2014), 185502.
[26] Q. Zeng, Y. Lin, Y. Liu, Z. Zeng, C.Y. Shi, B. Zhang, H. Lou, S.V. Sinogeikin, Y. Kono, C. Kenney-Benson, C. Park, W. Yang, W. Wang, H. Sheng, H.K. Mao, W.L. Mao, General 2.5 power law of metallic glasses, Proc. Natl. Acad. Sci. U.S.A. 113 (2016) 1714–1718.
[27] Q. Zheng, Y. Zhang, M. Montazerian, O. Gulbiten, J.C. Mauro, E.D. Zanotto, Y. Yue, Understanding glass through differential scanning calorimetry, Chem. Rev. 119 (2019) 7848–7939.
[28] P.P. Jana, A. Gunti, J. Das, Improvement of intrinsic plasticity and strength of Zr55Cu30Ni5Al10 metallic glass by tuning the glass transition temperature, Mater. Sci. Eng. A 762 (2019).
[29] X.H. Wang, A. Inoue, F.L. Kong, S.L. Zhu, M. Stoica, I. Kaban, C.T. Chang, E. Shalaan, F. Al-Marzouki, J. Eckert, Influence of ejection temperature on structure and glass transition behavior for Zr-based rapidly quenched disordered alloys, Acta Mater 116 (2016) 370–381.
[30] A.R. Yavari, A. Le Moulec, W.J. Botta F, A. Inoue, P. Rejmankova, A. Kvick, In situ crystallization of Zr55Cu30Al10Ni5 bulk glass forming from the glassy and undercooled liquid states using synchrotron radiation, J. Non·Cryst. Solids 247 (1999) 31–34.
[31] R.A. Sergiienko, O.A. Shcheretskyi, V.Y. Zadorozhnyy, A.M. Verkhovliuk, D. V. Louzguine-Luzgin, Investigation of Zr55Cu30Al10Ni5 bulk amorphous alloy crystallization, J. Alloys Compd. 791 (2019) 477–482.
[32] I. Seki, K. Wakoh, A. Kawashima, H. Kimura, A. Inoue, Preparation of a Wide Zr55Al10Ni5Cu30 metallic glass sheet by a twin-roller type casting method and its mechanical properties, Mater. Trans. JIM 47 (2006) 1926–1929.
[33] C. Chen, Y. Fan, W. Zhang, H. Zhang, R. Wei, S. Guan, T. Wang, T. Zhang, F. Li, Tailoring Nano-crystallization in Zr50Ti4Y1Al10Cu25Ni7Co2Fe1 complex multicomponent bulk metallic glass by O doping, J. Non·Cryst. Solids 553 (2021), 120474.
[34] Y. Yokoyama, T. Shinohara, K. Fukaura, A. Inoue, Characterization of crystalline inclusions in cast bulk Zr-Cu-Ni-Al glassy alloy, Mater. Trans. JIM 45 (2004) 1819–1823.
[35] Y. Yokoyama, K. Fukaura, A. Inoue, Cast structure and mechanical properties of Zr–Cu–Ni–Al bulk glassy alloys, Intermetallics 10 (2002) 1113–1124.
[36] M.L. Manning, A.J. Liu, Vibrational modes identify soft spots in a sheared disordered packing, Phys. Rev. Lett. 107 (2011), 108302.
[37] H.L. Peng, M.Z. Li, W.H. Wang, Structural signature of plastic deformation in metallic glasses, Phys. Rev. Lett. 106 (2011), 135503.
[38] E. Ma, Tuning order in disorder, Nat. Mater. 14 (2015) 547–552.
[39] S. Patinet, D. Vandembroucq, M.L. Falk, Connecting local yield stresses with plastic activity in amorphous solids, Phys. Rev. Lett. 117 (2016), 045501.
[40] A. Hirata, P. Guan, T. Fujita, Y. Hirotsu, A. Inoue, A.R. Yavari, T. Sakurai, M. Chen, Direct observation of local atomic order in a metallic glass, Nat. Mater. 10 (2011) 28–33.
[41] Y.H. Liu, D. Wang, K. Nakajima, W. Zhang, A. Hirata, T. Nishi, A. Inoue, M. W. Chen, Characterization of nanoscale mechanical heterogeneity in a metallic glass by dynamic force microscopy, Phys. Rev. Lett. 106 (2011), 125504.

[42] H. Wagner, D. Bedorf, S. Kuchemann, M. Schwabe, B. Zhang, W. Arnold, K. Samwer, Local elastic properties of a metallic glass, Nat. Mater. 10 (2011) 439–442.
[43] S. Lan, L. Zhu, Z. Wu, L. Gu, Q. Zhang, H. Kong, J. Liu, R. Song, S. Liu, G. Sha, Y. Wang, Q. Liu, W. Liu, P. Wang, C.T. Liu, Y. Ren, X.L. Wang, A medium-range structure motif linking amorphous and crystalline states, Nat. Mater 20 (2021) 1347–1352.
[44] K. Nomoto, A.V. Ceguerra, C. Gammer, B. Li, H. Bilal, A. Hohenwarter, B. Gludovatz, J. Eckert, S.P. Ringer, J.J. Kruzic, Medium-range order dictates local hardness in bulk metallic glasses, Mater. Today 44 (2021) 48–57.
[45] Z. Lu, A.K.A. Lu, F. Zhang, Y. Tian, J. Jiang, D. Wei, J. Han, Q. Gao, K. Ohara, H. Kato, A. Hirata, M. Chen, Crystal-like order stabilizing glasses: structural origin of ultra-stable metallic glasses, Preprint at https://arxiv.org/pdf/2111.02606.
[46] C. Jixiang, W. Qing, D. Chuang, Cluster Rule in Alloy Phase and Its Application in Zr-Al-Ni System, Rare Metal Mat. Eng. 40 (2011) 69–73.
[47] C.A. Teixeira, R.V. da Silva, L.T. Pereira, M.F. de Oliveira, Oxygen effect on bending behavior of a zirconium based bulk metallic glass, J. Non-Cryst. Solids 535 (2020), 119966.
[48] M. Baricco, S. Spriano, I. Chang, M. Petrzhik, L. Battezzati, Big cube" phase formation in Zr-based metallic glasses, Mater. Sci. Eng. A 304 (2001) 305–310.
[49] A. Inoue, High strength bulk amprphous alloys with low critical cooling rates (overview), Mater. Trans. JIM 36 (1995) 866–875.
[50] Z.P. Lu, C.T. Liu, Glass formation criterion for various glass-forming systems, Phys. Rev. Lett. 91 (2003), 115505.
[51] D. Turnbull, Under what conditions can a glass be formed? Contemp. Phys. 10 (1969) 473–488.
[52] H.E. Kissinger, Reaction kinetics in Differential Thermal Analysis, Anal. Chem. 29 (1957) 1702–1706.
[53] F.X. Qin, H.F. Zhang, B.Z. Ding, Z.Q. Hu, Nanocrystallization kinetics of Ni-based bulk amorphous alloy, Intermetallics 12 (2004) 1197–1203.
[54] H.R. Wang, Y.L. Gao, G.H. Min, X.D. Hui, Y.F. Ye, Primary crystallization in rapidly solidified Zr70Cu20Ni10 alloy from a supercooled liquid region, Phys. Lett. A 314 (2003) 81–87.
[55] Y.h. Li, W. Zhang, C. Dong, J.b. Qiang, A. Makino, Correlation between the glass-forming ability and activation energy of crystallization for Zr75-xNi25Alx metallic glasses, Int. J. Miner. Metall. 20 (2013) 445–449.
[56] Y. Yokoyama, E. Mund, A. Inoue, L. Schultz, Production of Zr 55 Cu 30 Ni 5 Al 10 Glassy Alloy Rod of 30mm in Diameter by a Cap-Cast Technique, Mater. Trans. JIM 48 (2007) 3190–3192.
[57] Z. Zhang, W. Zhou, X.Z. Xiong, L.T. Kong, J.F. Li, Glass forming ability and primary crystallization behavior of Al–Ni–Ce alloys, Intermetallics 24 (2012) 1–6.
[58] L. Yang, G.Q. Guo, L.Y. Chen, C.L. Huang, T. Ge, D. Chen, P.K. Liaw, K. Saksl, Y. Ren, Q.S. Zeng, B. LaQua, F.G. Chen, J.Z. Jiang, Atomic-scale mechanisms of the glass-forming ability in metallic glasses, Phys. Rev. Lett. 109 (2012), 105502.
[59] Y. Li, Q. Guo, J.A. Kalb, C.V. Thompson, Matching glass-forming ability with the density of the amorphous phase, Science 322 (2008) 1816–1819.
[60] X.K. Xi, L.L. Li, B. Zhang, W.H. Wang, Y. Wu, Correlation of atomic cluster symmetry and glass-forming ability of metallic glass, Phys. Rev. Lett. 99 (2007), 095501.
[61] D.P.B. Aji, A. Hirata, F. Zhu, L. Pan, K.M. Reddy, Y. Liu, T. Fujita, S. Kohara, M. Chen, Ultrastrong and Ultrastable Metallic Glass, Preprint at https://arxiv.org/pdf/1306.1575.
[62] Z.F. Zhang, J. Eckert, L. Schultz, Difference in compressive and tensile fracture mechanisms of Zr59Cu20Al10Ni8Ti3 bulk metallic glass, Acta Mater 51 (2003) 1167–1179.
[63] X.K. Xi, D.Q. Zhao, M.X. Pan, W.H. Wang, Y. Wu, J.J. Lewandowski, Fracture of brittle metallic glasses: brittleness or plasticity, Phys. Rev. Lett. 94 (2005), 125510.
[64] B.A. Sun, W.H. Wang, The fracture of bulk metallic glasses, Prog. Mater. Sci. 74 (2015) 211–307.
[65] A.J.A.m. Argon, Plastic deformation in metallic glasses, Acta Metall 27 (1979) 47–58.
[66] D.P. Wang, B.A. Sun, M. Gao, Y. Yang, C.T. Liu, The mechanism of shear-band blocking in monolithic metallic glasses, Mater. Sci. Eng. A 703 (2017) 162–166.
[67] M. Samavatian, R. Gholamipour, A.A. Amadeh, S. Mirdamadi, Role of tensile elastostatic loading on atomic structure and mechanical properties of Zr55Cu30Ni5Al10 bulk metallic glass, Mater. Sci. Eng. A 753 (2019) 218–223.